Materials and Structures
DOI 10.1617/s11527-014-0383-7

ORIGINAL ARTICLE

Influence of asphaltene content on mechanical bitumen behavior: experimental investigation and micromechanical modeling

Lukas Eberhardsteiner · Josef Füssl · Bernhard Hofko · Florian Handle · Markus Hospodka · Ronald Blab · Hinrich Grothe

Received: 14 January 2014 / Accepted: 15 July 2014

Abstract The description of the mechanical behavior of bitumen on the basis of its microstructure allows its improvement and moreover the development of equivalent or even more sustainable materials with similar properties. For this reasons, a micromechanical model for bitumen is proposed, allowing the description of the viscoelastic bitumen behavior depending on characteristics of different material phases. The definition and demarcation, respectively, of material phases is based on SARA fractions, and polarity considerations that support the assumption of asphaltene micelle structures within a contiguous matrix and the assumed interactions between them. A sufficient number of static creep tests on artificially composed bitumen samples with asphaltene contents from 0 to 30 wt% served both as identification as well as validation experiments for the developed micromechanical model. An excellent agreement between experimental results and model predictions indicates that the model is able to reproduce significant microstructural effects, such as interactions between asphaltenes, which strongly influence the bitumen behavior. This model is therefore expected to contribute to a better understanding of the influence of the bitumen microstructure on the macroscopic mechanical behavior and subsequently be able to describe the mechanical consequences of microstructural effects like aging.

Keywords Bitumen · Microstructure · Multiscale · SARA fractions · Viscoelasticity · DSR

L. Eberhardsteiner (✉) · B. Hofko · M. Hospodka · R. Blab
Institute of Transportation - Research Center for Road Engineering, Vienna University of Technology, Gusshausstraße 28/230/3, 1040 Vienna, Austria
e-mail: lukas.eberhardsteiner@tuwien.ac.at

J. Füssl
Institute for Mechanics of Materials and Structures, Vienna University of Technology, Karlsplatz 13/202, 1040 Vienna, Austria
e-mail: josef.fuessl@tuwien.ac.at

F. Handle · H. Grothe
Institute of Materials Chemistry, Vienna University of Technology, Getreidemarkt 9/BC/02, 1060 Vienna, Austria
e-mail: florian.handle@tuwien.ac.at

Published online: 06 August 2014

1 Introduction

In times of a predictable shortage of crude oil, researchers all over the world focus on the development of alternatives to petroleum products, like bitumen, a distillation product of crude oil and mainly used as binder in hot mix asphalt (HMA). Due to its natural origin, there is a significant variability in its composition and material behavior depending on the crude oil source. Moreover, a huge number of molecules with very different chemical structure build up bitumen and makes it one of the most complex

building materials. For this reason, a detailed understanding of the mechanical behavior triggered by the microstructure of bitumen is a challenging task, but needed to support sustainable use and repeated recycling.

In recent years, multiscale modeling came up to predict the mechanical behavior of composite materials like wood, concrete, bone or HMA [12, 14, 20, 21, 27, 37] on the basis of observations of their microstructures. Lackner et al. [21, 22], Aigner et al. [1], Pichler and Lackner [31] and Pichler et al. [33] introduced such a model to predict the viscoelastic material behavior of asphalt concrete. Thereby, the material structure is defined through five scales of observation and appropriate homogenization schemes link the mechanical properties from the lowest (bitumen) scale up to the macrolevel. At each observation scale, the characteristics of the constituents are derived either from homogenizing the material behavior at the scale below or are obtained from identification experiments at the respective scale. Characteristics of the constituents like morphology, volume content or interaction between the material phases are considered in the framework of continuum micromechanics. This homogenization process leads to an overall material characterization of asphalt concrete. As logical and consistent next step, the extension of this model to the microstructure of bitumen is proposed in this paper.

The most common procedure to identify the constituents of bitumen chemically is saturates, aromatics, resins and asphaltenes (SARA) fractionation. At first, bitumen is separated in maltenes, the fraction soluble in n-heptane, and asphaltenes, the non-soluble parts [35]. Using chromatographic separation methods according to ASTM Standard 4124 [2], (see also [6, 25]) maltenes can be further separated into saturates, aromatics and resins [25, 36]. Saturates look like a colorless or slightly colored oily liquid at room temperature (see Fig. 1) and represent between about 5 and 15 wt% of paving grade bitumen [25]. Aromatics and resins contribute to a large extend to bitumen (30–45 wt% each). While aromatics form a yellow to red oily liquid at room temperature (see Fig. 1) and are mainly responsible for the viscous behavior of bitumen, resins form a black solid and play an important role in stabilizing asphaltenes within bitumen [25]. At room temperature, asphaltenes form a black powder and are responsible for the black color of bitumen.

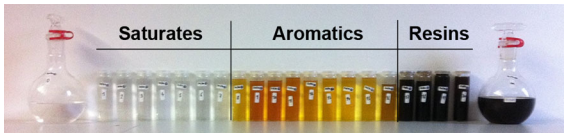

Fig. 1 Maltene fractions (saturates, aromatics and resins) from chromatography according to modified ASTM Standard 4124 [2]

They account for about 5–20 wt% of paving grade bitumen.

Confocal Laser Scanning Microscopy (CLSM) or Atomic Force Microscopy (AFM) are imaging methods, which allow to access the microstructure of materials like bitumen. From the results of these tests, a heterogeneous characteristic of the bitumen microstructure, consisting of micelle-like structures embedded into a matrix, could be confirmed [16]. The origin of these heterogeneity is subject of an ongoing debate in bitumen research [25]. While some authors believe that waxes are responsible for the microstructure of bitumen [26, 30], in this work asphaltenes—together with resins and aromatics—are assumed to form micelle structures [3, 5, 10, 11, 25, 43], which strongly contribute to the stiffness of bitumen. First experiments on bitumen with an artificially reduced saturate content have shown an increase in stiffness and therefore support this assumption.

Based on these assumptions, within this paper, a micromechanical model allowing for the mechanical description of the bitumen behavior depending on its composition is presented. First, identification experiments on artificial bitumen with varying asphaltene content were conducted and evaluated. In consequence, the developed micromechanical model is presented and discussed in detail. In addition, the basic continuum micromechanical relations are provided. Then, model predictions and test results are compared to validate the developed model approach, before, finally, conclusions are drawn.

2 Experiments

As outlined, bitumen can be separated into asphaltenes and maltenes because of a difference in solubility in n-heptane. While maltenes form a relatively low-viscous matrix, asphaltenes appear as highly viscous

Table 1 Experimental program for CR tests on artificially mixed bitumen

Asphaltene content		Test temperature		
		−5 °C	+5 °C	+15 °C
0	0 vol%	•	•	•
5 wt%	4.18 vol%	•	•	•
10 wt%	7.77 vol%		•	
15 wt%	12.32 vol%		•	•
20 wt%	17.36 vol%		•	
30 wt%	26.71 vol%		•	

and very stiff inclusions dispersed in the maltene phase. In order to identify the influence of microstructural changes, artificial bitumens were produced from a paving grade bitumen 70/100 with 7.79 vol% asphaltene content. After separating maltenes and asphaltenes by n-heptane and evaporating the solvent, asphaltenes and maltenes were dissolved in toluene. By mixing these solutions again with different proportions and evaporating the toluene, asphaltenes can be "re-dispersed" in the maltene phase. In that way, artificial bitumens with varying asphaltene content from 0 to 30 wt% were produced. Taking the density of asphaltenes and maltenes into account, this is equivalent to 0–26.71 vol% (see Table 1). In the following, only vol% are used and labelled as %.

The material behavior of these mixtures was identified through a so-called Creep–Recovery (CR) test, a static shear creep test performed on the experimental setup of a dynamic shear rheometer (DSR) (see Fig. 2).

Instead of an oscillating loading through the upper plate, a constant torque M is applied statically for 1,800 s, so that a predefined maximum shear stress $\tau = 2M/\pi r^3$, with $r = d/2$, is obtained. The loading plate has a diameter of $d = 25$ mm and the bitumen film has a constant height of $h = 1$ mm. Within a conditioning phase of 600 s, the samples were tempered to a predefined test temperature in the range of −5 to +15 °C. From the strain γ,

$$\gamma(t) = \frac{r}{\pi}\varphi(t) \tag{1}$$

with the measured deflection $\varphi(t)$, the creep compliance is obtained according to

$$J_{\exp}(t) = \frac{\gamma(t)}{\tau}. \tag{2}$$

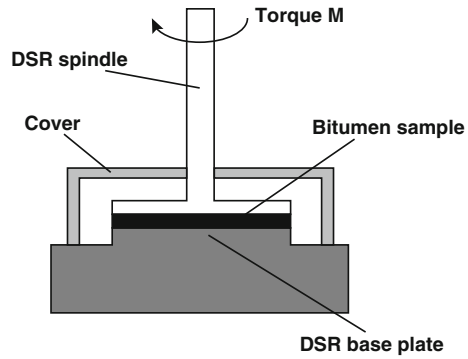

Fig. 2 CR test using DSR experimental equipment

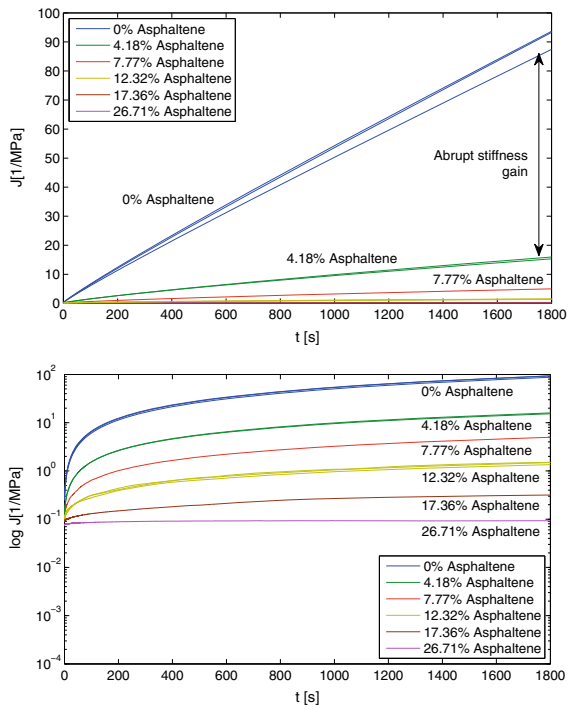

Fig. 3 Results from CR tests on artificially mixed bitumen at +5 °C on a linear (*upper*) and a logarithmic scale (*lower*)

The full experimental program is given in Table 1.

Figure 3 shows the results of the CR tests for artificial bitumen samples with various asphaltene contents at +5 °C. As shown in this figure, increasing asphaltene content causes a decrease in creep compliance and hence stiffer material behavior. In addition, the creep rate dJ/dt decreases with increasing asphaltene content, until almost elastic behavior is reached at an asphaltene content of 26.71 %. It is noticeable that there is an abrupt increase in stiffness, when only low

amounts of asphaltenes (4.18 %) are added to the maltene phase (see Fig. 3). This already indicates that by adding asphaltenes a structure in bitumen is introduced, which strongly affects the mechanical behavior.

These tests also served as identification experiments to determine the material behavior of the maltene phase, as will be described in Sect. 4.

3 Micromechanical model of bitumen

In order to be able to understand the mechanical behavior of composite materials (like bitumen), taking a look at the material's microstructure seems essential. A modeling technique capable of taking the composition of a material into account, is multiscale modeling using the framework of continuum micromechanics [18, 19, 37, 41, 44, 45] on each scale of observation. There, a material is understood as a micro-heterogenous body filling a macro-homogeneous representative volume element (RVE). Quasi-homogenous subdomains (material phases) [41, 44, 45] with known physical properties, like volume fractions and elastic/viscoelastic properties, are reasonably chosen, as to describe the complex microstructure within an RVE. The size of the inhomogeneities defined by the material phases has to be significantly smaller than the characteristic length of the RVE, and, the size of the RVE again has to be smaller than the characteristic dimension of the structure built up by the material.

Considering the elastic/viscoelastic behavior of the material phases within the RVE, as well as the volume fractions, their characteristic shapes and their interactions, the homogenized mechanical behavior of the overall material can be estimated in terms of a correlation between homogeneous deformations acting on the boundary of the RVE and resulting (average) stresses.

If a single phase has a heterogeneous microstructure itself, RVEs can be introduced within this phase in order to estimate its mechanical behavior. Naturally, the dimensions of these RVEs have to be significantly smaller than the RVE built up by the phase itself, and imply again smaller inhomogeneities with smaller characteristic lengths, and so on. This approach leads to a multistep homogenization scheme, as employed for asphalt in [1, 21, 22, 31, 33]. To extend the model to the microstructure of bitumen is the very focus of the present paper.

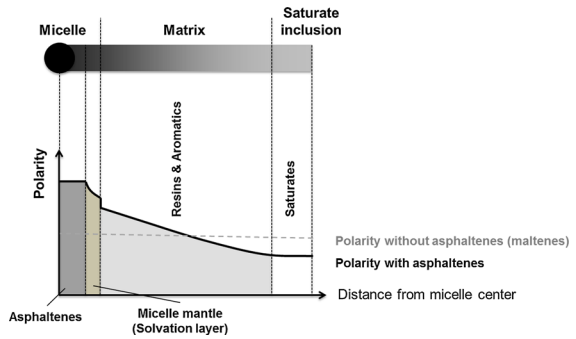

Fig. 4 Schematic illustration of the polarity evolution over the different material phases in bitumen

3.1 Concept of material phases

Thereby, the main challenge is an appropriate choice of number and characteristics of material phases. A too detailed representation of the microstructure is not useful due to little knowledge of the structural composition and missing properties of single phases. Nevertheless, a sufficient number of material phases must be differentiated and their interactions considered to capture the main structural effects influencing the mechanical behavior of bitumen. It is assumed that a structural concept based on the SARA fractions can meet this requirements. Accordingly bitumen is separated in saturates, aromatics, resins and asphaltenes (SARA fractions) [25, 35, 36]. As the separation within chromatographic methods is based on the fact, that chemically different constituents differ in polarity, the demarcation of the individual phases as well as structural effects in bitumen can be explained by qualitative polarity distributions over a representative volume of bitumen (see Fig. 4). While the maltene phase exhibits a constant level of polarity overall (see grey dashed line in Fig. 4), its constituents differ in polarity, rising from saturates via aromatics to resins. When adding highly polar asphaltenes, resins and aromatics adhere to the asphaltenes and form a solvation layer (mantle) around them leading to a micelle structure [25], which smothers the difference in polarity between asphaltenes and surrounding maltenes and thus helps to stabilize the asphaltenes within the maltene matrix (see black line in Fig. 4).

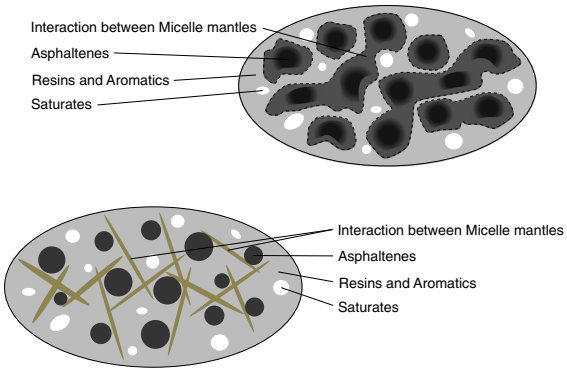

Fig. 5 Microstructural concept of bitumen based on SARA fractions and polarity considerations (*upper*) and derived structural RVE concept for micromechanical modeling (*lower*)

These micelle mantles interact with each other dependent on the volume fraction of asphaltenes and form a network-like structure (see Fig. 5, upper), which could serve as a feasible explanation for the abrupt stiffness gain seen in Fig. 3.

The identified material phases, building the microstructure of bitumen, are implemented in a homogenization scheme predicting the overall mechanical behavior of bitumen (see Fig. 5, lower). An RVE of bitumen is built up by a contiguous matrix of aromatics and resins (labelled by suffix "arom") with embedded spherical saturate inclusions (suffix "sat"). While asphaltenes ("aspha") also form spherical inclusions in the maltene matrix [25], the network structure formed by the micelle mantles is represented by an interaction phase ("ip") appearing as needles, being oriented in all directions.

As identification experiments are only available for maltenes (saturates, aromatics and resins), in a first step saturate inclusions and aromatics-resin matrix are assumed to exhibit the same viscoelastic behavior (see also Sect. 3.2). Furthermore, asphaltenes and their mantles are considered as different phases with respect to volume content and morphology but assumed to show the same viscoelastic response because of acting together in the micelle structure.

3.2 Description of viscoelastic behavior

As described before, the constituents of bitumen exhibit viscoelastic behavior, for which the relation between stresses and strains can be written as follows

$$\boldsymbol{\sigma}_i(t) = \int_{-\infty}^{t} \mathbf{r}_i(t-\tau) : \dot{\boldsymbol{\varepsilon}}_i(\tau)\ \mathrm{d}\ \tau = [\mathbf{r}_i * \boldsymbol{\varepsilon}_i](t) \tag{3}$$

where $\dot{\boldsymbol{\varepsilon}}_i$ denotes the temporal derivative of the strain tensor of material phase i, $\mathbf{r}_i(t-\tau)$ is the fourth-order tensorial relaxation function, τ is the integration variable related to the time instant when $\dot{\boldsymbol{\varepsilon}}_i$ was imposed onto the material phase, and $*$ represents the Stieltjes convolution operator. Thereby, $\mathbf{r}_i(t=\tau)$ refers to instantaneous elasticity, while $\mathbf{r}_i(t>\tau)$ refers to viscoelastic deformations. For reasons of convenience, Eq. (3) is represented in the Laplace Carson (LC) domain defined through frequency variable p, with the LC transformation reading [8],

$$f^*(p) = \mathcal{C}\{f(t)\} = p\hat{f}(p) = p\int_0^{\infty} f(t)e^{-pt}\mathrm{d}t, \tag{4}$$

where $f^*(p)$ is the LC transform of the time-dependent function $f(t)$ and $\hat{f}(p)$ is the Laplace transform of $f(t)$. Inserting Eq. (3) into Eq. (4) yields an algebraic equation in the LC domain, given as

$$\boldsymbol{\sigma}_i^*(p) = \mathbf{r}_i^*(p) : \boldsymbol{\varepsilon}_i^*(p). \tag{5}$$

As bitumen is an isotropic material, isotropic behavior can also be assumed for the material phases within the RVE, so that their relaxation tensors read

$$\mathbf{r}_i^*(p) = 3K_i^*(p)\mathbf{I}_{\mathrm{vol}} + 2\mu_i^*(p)\mathbf{I}_{\mathrm{dev}}, \tag{6}$$

with $\mathbf{I}_{\mathrm{vol}}$ as the volumetric part of the fourth-order unity tensor $\mathbf{I}$, with components $I_{\mathrm{vol},ijkl} = 1/3\delta_{ij}\delta_{kl}$ and Kronecker delta δ_{ij} ($\delta_{ij} = 1$ if $i = j$, and $\delta_{ij} = 0$ if $i \neq j$), while $\mathbf{I}_{\mathrm{dev}}$ represents the deviatoric part of the fourth-order unity tensor $\mathbf{I}$ ($\mathbf{I}_{\mathrm{dev}} = \mathbf{I} - \mathbf{I}_{\mathrm{vol}}$). The components of $\mathbf{I}$ are defined as $I_{ijkl} = 1/2(\delta_{ik}\delta_{jl} + \delta_{il}\delta_{jk})$. The bulk modulus of all material phases is independent of p, and hence identical to the elastic bulk modulus, $K_i^* \equiv K_i$. Due to the incompressibility of bitumen and its constituents (Poisson ratio $\nu = 0.5$), K_i is assumed to be magnitudes higher than the elastic modulus approximating infinity. The shear modulus μ_i^* is defined as $\mu_i^* = 1/J_i^*$, with the shear compliance J_i^* according to the power-law model, best applicable to describe the viscoelastic material behavior of bitumen [1], reading

$$J_i^*(p) = J_{0,i} + J_{\mathrm{a},i}(p\bar{\tau})^{-k_i}\Gamma(1+k_i), \tag{7}$$

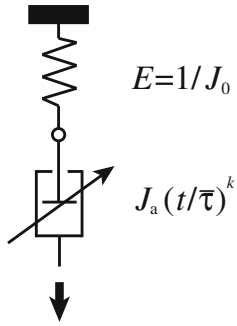

Fig. 6 Power-law model

where $J_{0,i}$ is the elastic shear compliance of phase i, and $J_{a,i}$ and k_i are viscous parameters (see Fig. 6).

3.3 Homogenization scheme for bitumen

Due to the formally linear elastic constitutive Eq. 5, the superposition principle is valid in the LC domain resulting in LC-transformed macroscopic strains $\mathbf{E}_{\mathrm{i}}^{*}(p)$ being proportional to LC-transformed microscopic strains in phase i, reading

$$\boldsymbol{\varepsilon}_i^{*}(p) = \mathbf{A}_i^{*}(p) : \mathbf{E}_{\mathrm{bit}}^{*}(p), \tag{8}$$

where $\mathbf{A}_i^{*}(p)$ denotes the LC-transformed fourth-order strain concentration tensor of phase i. Equation 8 refers to the viscoelastic correspondence principle [4, 24, 34, 38]. Insertion of Eq. 8 into Eq. 5 and considering formally elastic matrix-inclusion problems of the Eshelby–Laws type [9, 23] define the LC-transformed homogenized relaxation tensor, in general reading as

$$\mathbf{R}^{*,\mathrm{est}} = \sum_r f_r \mathbf{r}_r^{*} : \left[\mathbf{I} + \mathbf{P}_r^{*,0}\left(\mathbf{r}_r^{*} - \mathbf{r}^{*,0}\right)\right]^{-1} : \left\{\sum_s f_s \left[\mathbf{I} + \mathbf{P}_s^{*,0} : \left(\mathbf{r}_s^{*} - \mathbf{r}^{*,0}\right)\right]^{-1}\right\}^{-1}, \tag{9}$$

with f_r and $\mathbf{r}_r^{*}$ as the volume fraction and relaxation tensor of phase r. Both sums are taken over all phases appearing in the heterogeneous RVE. The characteristic shape of phase r is considered through the fourth-order Hill tensor $\mathbf{P}^{*,0}$, which depends on the relaxation tensor $\mathbf{r}^{*,0}$ of the surrounding phase. The interaction between phases is described by a Mori–Tanaka scheme [28, 42], typical for composite materials consisting of a contiguous matrix with inclusions. Considering the relaxation function in Eq. 6, the homogenization of an RVE of bitumen can be carried out on the basis of a p-related, continuos sequence of formally elastic problems of the type of Eq. 9, delivering homogenized relaxation tensors $\mathbf{R}_{\mathrm{bit}}^{*}(p)$, reading as

$$\begin{aligned}
\mathbf{R}_{\mathrm{bit}}^{*}(p) = \Big\{ & \left(1 - f_{\mathrm{aspha}} - f_{\mathrm{ip}} - f_{\mathrm{sat}}\right)\mathbf{r}_{\mathrm{arom}}^{*}(p). \\
& + f_{\mathrm{aspha}}\mathbf{r}_{\mathrm{aspha}}^{*}(p)^{*} : \Big[\mathbf{I} + \mathbf{P}_{\mathrm{sph}}^{*,\mathrm{arom}}(p) : \\
& \left(\mathbf{r}_{\mathrm{aspha}}^{*}(p) - \mathbf{r}_{\mathrm{arom}}^{*}(p)\right)\Big]^{-1} + f_{\mathrm{ip}}\mathbf{r}_{\mathrm{ip}}^{*}(p) \\
& : \int_{\varphi=0}^{2\pi}\int_{\vartheta 0}^{\pi} \Big[\mathbf{I} + \mathbf{P}_{\mathrm{cyl}}^{*,\mathrm{arom}}(\vartheta,\varphi,\mathrm{p}) : \\
& \left(\mathbf{r}_{\mathrm{ip}}^{*}(p) - \mathbf{r}_{\mathrm{arom}}^{*}(p)\right)\Big]^{-1} \frac{\sin\vartheta d\vartheta d\varphi}{4\pi} \\
& + f_{\mathrm{sat}}\mathbf{r}_{\mathrm{sat}}^{*}(p) : \Big[\mathbf{I} + \mathbf{P}_{\mathrm{sph}}^{*,\mathrm{arom}}(p) : \\
& \left(\mathbf{r}_{\mathrm{sat}}^{*}(p) - \mathbf{r}_{\mathrm{arom}}^{*}(p)\right)\Big]^{-1}\Big\} : \\
& \Big\{\left(1 - f_{\mathrm{aspha}} - f_{\mathrm{ip}} - f_{\mathrm{sat}}\right)\mathbf{I} \\
& + f_{\mathrm{aspha}} \cdot \Big[\mathbf{I} + \mathbf{P}_{\mathrm{sph}}^{*,\mathrm{arom}}(p) : \left(\mathbf{r}_{\mathrm{aspha}}^{*}(p) - \mathbf{r}_{\mathrm{arom}}^{*}(p)\right)\Big]^{-1} \\
& + f_{\mathrm{ip}} \int_{\varphi=0}^{2\pi}\int_{\vartheta=0}^{\pi} \Big[\mathbf{I} + \mathbf{P}_{\mathrm{cyl}}^{*,\mathrm{arom}}(\vartheta,\varphi,\mathrm{p}) : \\
& \left(\mathbf{r}_{\mathrm{ip}}^{*}(p) - \mathbf{r}_{\mathrm{arom}}^{*}(p)\right)\Big]^{-1} \frac{\sin\vartheta d\vartheta d\varphi}{4\pi} \\
& + f_{\mathrm{sat}}\Big[\mathbf{I} + \mathbf{P}_{\mathrm{sph}}^{*,\mathrm{arom}}(p) : \left(\mathbf{r}_{\mathrm{sat}}^{*}(p) - \mathbf{r}_{\mathrm{arom}}^{*}(p)\right)\Big]^{-1}\Big\}^{-1}
\end{aligned} \tag{10}$$

For the definition of the fourth-order Hill tensors $\mathbf{P}_{\mathrm{sph}}^{*,\mathrm{arom}}$ and $\mathbf{P}_{\mathrm{cyl}}^{*,\mathrm{arom}}$, which depend on the relaxation tensor $\mathbf{r}_{\mathrm{arom}}^{*}$ of the surrounding phase (resins and aromatics), see [9] and [13]. The integrals in Eq. 10 account for needles representing the interaction phase oriented in all directions and can be solved very efficiently with the help of Stroud's integration formula [32, 40]

$$\begin{aligned}
& \int_{\varphi=0}^{2\pi}\int_{\vartheta=0}^{\pi} \Big[\mathbf{I} + \mathbf{P}_{\mathrm{cyl}}^{*,\mathrm{arom}}(\vartheta,\varphi,\mathrm{p}) : \left(\mathbf{r}_{\mathrm{ip}}^{*}(p) - \mathbf{r}_{\mathrm{arom}}^{*}(p)\right)\Big]^{-1} \\
& \frac{\sin\vartheta \mathrm{d}\vartheta \mathrm{d}\varphi}{4\pi} = \sum_{j=0}^{n} \omega(\vartheta_j,\varphi_j)\Big[\mathbf{I} + \mathbf{P}_{\mathrm{cyl}}^{*,\mathrm{arom}}(\vartheta_j,\varphi_j,\mathrm{p}) : \\
& \left(\mathbf{r}_{\mathrm{ip}}^{*}(p) - \mathbf{r}_{\mathrm{arom}}^{*}(p)\right)\Big]^{-1}.
\end{aligned} \tag{11}$$

For the scalar weights $\omega(\vartheta_j, \varphi_j)$ see Appendix 1, the determination of $\mathbf{P}_{\text{cyl}}^{*,\text{arom}}(\vartheta_j, \varphi_j, \text{p})$ is given in Appendix 2.

In order to describe the creep response of bitumen in a physically relevant format, the LC-transformed creep tensor has to be determined, using

$$\mathbf{J}_{\text{bit}}^{*} = [\mathbf{R}_{\text{bit}}^{*}]^{-1}, \tag{12}$$

from which the component $J_{4444}^{*}(p)$ can be back-transformed into the time domain employing the Gaver–Stehfest algorithm as outlined in [39] to obtain the shear creep compliance $J_{\text{bit}}(t)$ allowing a comparison with the measured experimental result $J_{\text{exp}}(t)$ according to Eq. 2.

3.4 Influence of asphaltene behavior on bitumen creep properties

As outlined in Sect. 3.1, the material behavior of asphaltenes and the interaction phase are assumed to exhibit the same viscoelastic behavior. While the parameters J_0, J_a and k for maltenes can be determined directly from identification experiments (as presented in Sect. 2), the material behavior of the asphaltene micelles can not be identified directly. Therefore, the material properties are back-calculated from experimental results on a best-fit basis (see Sect. 4 for details).

In advance, the influence of the asphaltene behavior on the overall creep properties of bitumen is analyzed to find out realistic magnitudes of the material properties and to develop an idea of the influence of these properties on the bitumen behavior. Therefore, the asphaltene parameters $J_{0,\text{aspha}}$, $J_{a,\text{aspha}}$ and k_{aspha} are varied separately within the ranges given in Table 2, while all other model input parameters are kept constant.

The basic conclusions of this parameter study are:

- Low values for the elastic compliance $J_{0,\text{aspha}} \leq 10^{-3}$ (1/MPa) (two magnitudes lower than $J_{0,\text{malt}}$), describing a very stiff material behavior of asphaltenes compared to maltenes, have no significant influence on the predicted bitumen creep response (see Fig. 7a). Figure 7b describes the homogenized creep compliance J at 1,800 s for different values of $J_{0,\text{aspha}}$, showing insignificant changes below 10^{-3}.
- The same phenomenon can be reported for values of the viscous parameter $J_{a,\text{aspha}}$ lower than 10^{-5} (1/MPa) (two magnitudes lower than $J_{a,\text{malt}}$; see Fig. 8b). In addition, a tendency to very stiff, elastic, and hence unrealistic bitumen behavior can be seen for decreasing values of $J_{a,\text{aspha}}$ (see Fig. 8a).
- Generally, the viscous parameter k_{aspha} has less influence on the overall viscous behavior than $J_{a,\text{aspha}}$. The predicted behavior becomes again unrealistic (very stiff, elastic), when k_{aspha} tends to 0 (see Fig. 9a). Values for k_{aspha} lower than 0.4 cause only insignificant changes in the homogenized creep behavior (see Fig. 9b).

Besides the behavior of the material phases, the volumetric composition of an RVE plays an important role in predicting the homogenized creep response. While the volume fractions of the asphaltenes are known from assembling the artificial bitumen, the volume fractions of the interaction phase, f_{ip}, has to be determined from back-calculation (see Sect. 4 for details). Therefore, the influence of the needle content on the predicted behavior is also analyzed in a parameter study. While the remaining model input parameters are kept constant, f_{ip} is varied within the range given in Table 2.

Figure 10 shows the expected increase in stiffness for increasing needle content. In addition, an abrupt stiffness gain can be observed, when adding only low amounts of needles comparable to the measured stiffness increase in Fig. 3. This provides a first evidence that the proposed multiscale model for bitumen is able to predict the viscoelastic behavior reliably. In the following section, the power-law model is validated and multiscale predictions and test results are compared.

Table 2 Upper and lower boundaries for parameter study of $J_{0,\text{aspha}}$, $J_{a,\text{aspha}}$, k_{aspha} and f_{ip}

Parameter	Lowest value	Highest value	Increment
$J_{0,\text{aspha}}$ (1/MPa	10^{-6}	1	10^{-1}
$J_{a,\text{aspha}}$ (1/MPa	10^{-7}	10^{-3}	10^{-1}
k_{aspha} (–)	0.1	0.9	0.1
f_{ip} (%)	0	10	1

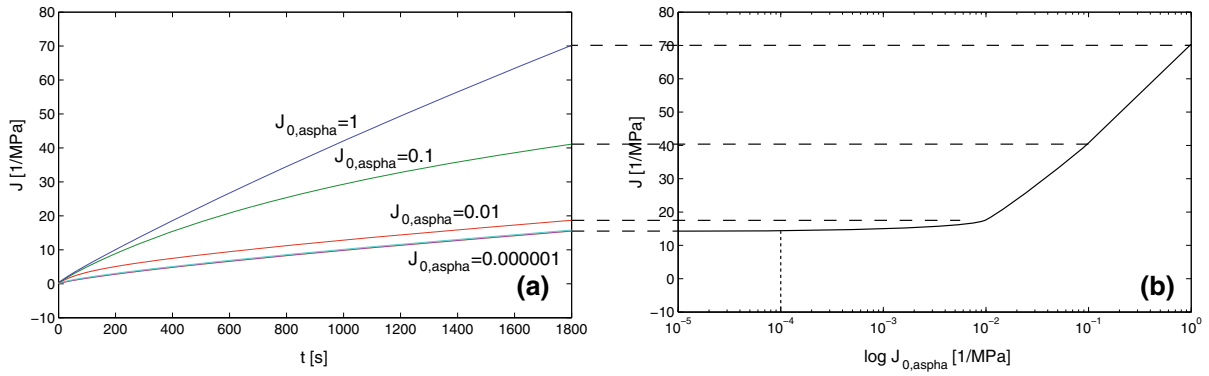

Fig. 7 Effect of a variation of $J_{0,\text{aspha}}$ on predicted bitumen behavior ($10^{-6} \leq J_{0,\text{aspha}} \leq 1$, by 10^{-1})

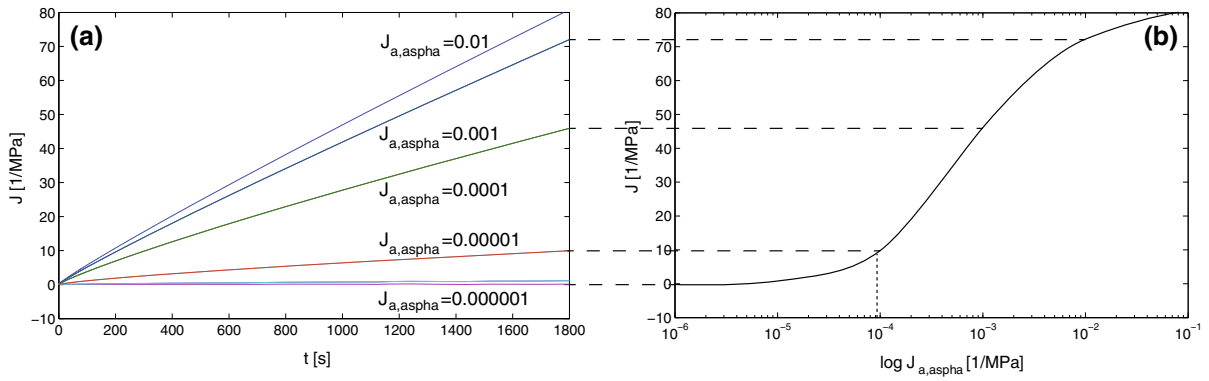

Fig. 8 Effect of a variation of $J_{\text{a,aspha}}$ on predicted bitumen behavior ($10^{-6} \leq J_{\text{a,aspha}} \leq 10^{-2}$, by 10^{-1})

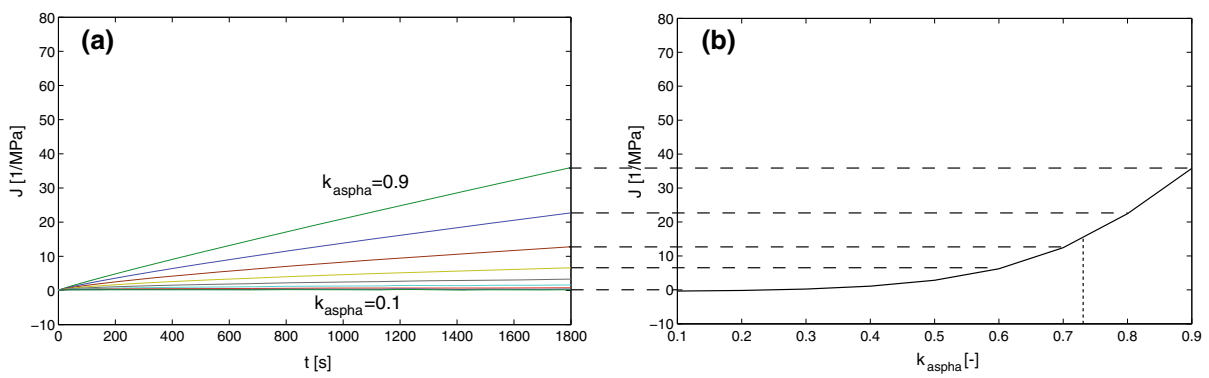

Fig. 9 Effect of a variation of k_{aspha} on predicted bitumen behavior ($0.1 \leq k_{\text{aspha}} \leq 0.9$, by 0.1)

4 Comparison of model predictions and test results

In Sect. 3.2, the power-law model, which is used to describe the viscoelastic response of bitumen and its constituents is presented. The parameters J_0, J_a and k are identified through minimizing the error—using nonlinear least square fitting—between experimentally obtained creep compliances J_{exp} from CR identification tests and predicted creep compliances J_{mod} in the time domain, reading [15]

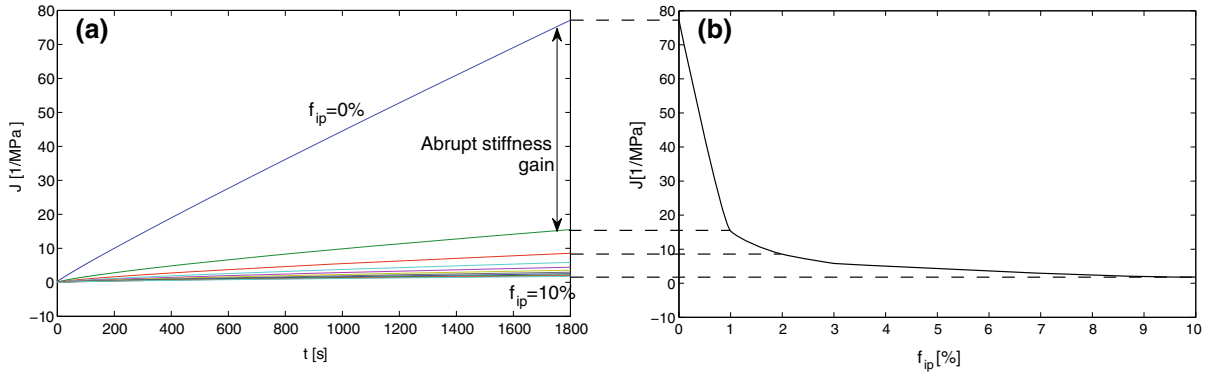

Fig. 10 Effect of a variation of the needle content f_{ip} on predicted bitumen behavior ($0\,\% \leq f_{ip} \leq 10\,\%$, by $1\,\%$)

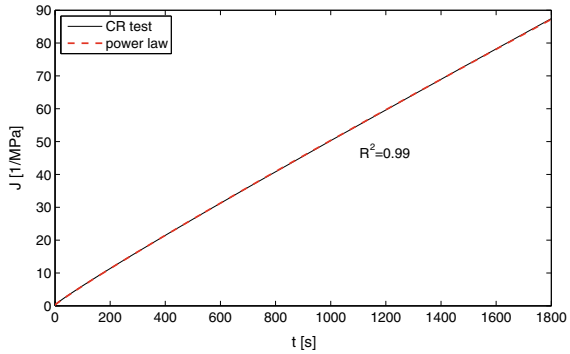

Fig. 11 CR-experimental results for maltene phase of bitumen at +5 °C and fitted power-law model

Table 3 Power-law parameters for maltene phase at −5, +5 and +15 °C

	−5 °C	+5 °C	+15 °C
$J_{0,\mathrm{malt}}$ (1/MPa)	0.0980	0.2652	2.433
$J_{a,\mathrm{malt}}$ (1/MPa)	0.0076	0.0766	1.205
k_{malt} (–)	0.8124	0.9386	1.027
R^2	0.99	0.99	0.99

$$J_{\mathrm{mod}} = J_0 + J_a \left(\frac{t}{\bar{\tau}}\right)^k. \tag{13}$$

This model is able to describe the experimentally obtained maltene behavior almost perfectly, as shown-for example for the maltene phase at +5 °C in Fig. 11. The obtained power-law parameters at −5, +5 and +15 °C are given in Table 3.

With the maltene material behavior at hand, the multiscale model introduced in Sect. 3.1 is able to

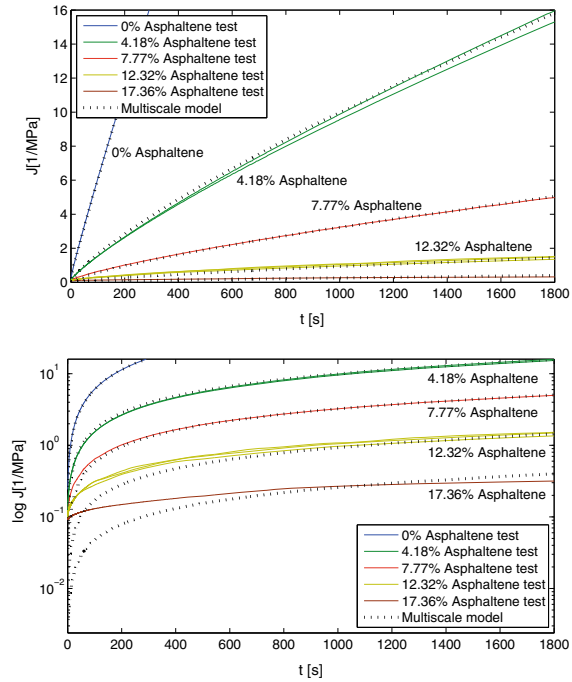

Fig. 12 Comparison of experimental results and multiscale model predictions for asphaltene contents of 4.18, 7.7, 12.32 and 17.36 at.% + 5 °C on a linear (*upper*) and a logarithmic scale (*lower*)

predict the creep response of bitumen using back-calculated asphaltene properties from experimental results for the artificial bitumen with 4.18 % asphaltenes. The parameters $J_{0,\mathrm{aspha}}$ and $J_{a,\mathrm{aspha}}$ lie within the range, where they only influence the homogenized material behavior insignificantly (see dotted lines in Figs. 7b and 8b in Sect. 3.4). To assure reliable model predictions, attention has to be paid when determining

Table 4 Correlation between asphaltene content and needle content representing interactions between micelles

Asphaltene content (%)	Content of interaction phase f_{ip} (%)
4.18	1
7.77	3.4
12.32	11
17.36	30

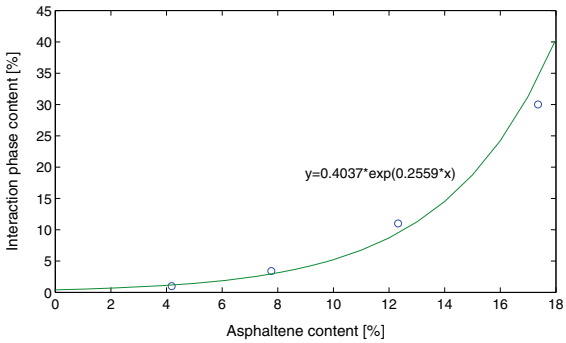

Fig. 13 Exponential relation between asphaltene and content of interaction phase

k_{aspha} (see Fig. 9). Therefore, the coefficient of determination, R^2, was used as an indicator for the degree of accordance. In addition, the volume fraction of the interaction phase is determined on a best-fit basis also using R^2 to evaluate the degree of accordance. In Fig. 12, model-predicted and experimental results are given for asphaltene contents of 4.18, 7.77, 12.32 and 17.36 %. Besides the known volume fraction of the asphaltenes, the content of the interaction phase was the only input parameter varied.

A very good accordance between experimental results and the viscoelastic response predicted by the proposed micromechanical model can be seen. The back-determined contents of the interaction phase are given in Table 4. When correlating asphaltene and needle content, an exponential relation can be found for (realistic) asphaltene contents between 0 and 17.36 % (see Fig. 13), not unlikely for molecular agglomeration processes in nature.

The material properties of the maltene phase is known for temperatures between −5 and +15 °C, as given in Table 3. Since the temperature dependency of the material behavior of bitumen follows an Arrhenius-type law of the form

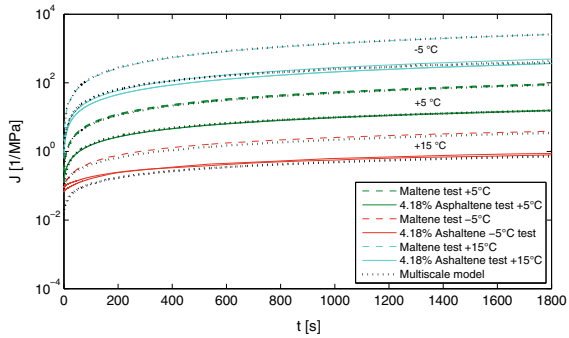

Fig. 14 Experimental results and model predictions for artificial bitumen with 4.18 % asphaltene content at −5, +5 and +15 °C

$$J(T) = J^0 exp\left[-\frac{E_a}{R}\left(\frac{1}{T}-\frac{1}{T_0}\right)\right], \tag{14}$$

where E_a is the activation energy, R is the gas constant, with $R = 8.31$ J/Mol/K, and T_0 is the reference temperature, it seems likely that its constituents also exhibit Arrhenius-type viscoelastic behavior. Hence, the temperature dependent properties of asphaltenes can be estimated from the change of behavior of the maltene phase at −5 to +15 °C. The model input parameters (material behavior of all constituents, volumetric composition and needle content) at hand, the overall creep response can be predicted for different temperatures (see Fig. 14) showing a remarkable accordance of model predictions and experimental results and, thus, indicating reasonably assumed values of the volume content of the interaction phase in Table 4.

5 Conclusion

By investigating bitumen chemically and rheologically, bitumen microstructure was identified to better understand how bitumen reacts mechanically. A first approach of predicting the viscoelastic reponse of bitumen respecting the volumetric composition and the mechanical behavior of its constituents has been proposed in this manuscript.

In order to observe bitumen microstructure experimentally, artificial bitumens with varying asphaltene content from 0 to 26.71 vol% were produced and analyzed in CR tests, a static shear creep experimental setup. As expected, an increase in asphaltene content

resulted in decreasing creep compliance and hence stiffer material behavior. Surprisingly, adding only low amounts of asphaltenes (from 0 to 4.18 vol%) caused an abrupt increase in stiffness indicating structural effects within bitumen.

A comparison between the original and the artificially composed bitumen samples show similar reactions in terms of linear viscoelastic behavior. Together with AFM analysis showing clear evidence of restoration of characteristic microstructural features known from bituminous binders (bee structures within a continuous matrix), this indicates that the artificial binders are valid bitumen-like materials and, thus, could reasonably be used for further mechanical analysis. These arguments will be presented in detail in further publication.

Due to its capability of respecting the volumetric composition of a composite material and the physical properties of its constituents—in other words the microstructure of a composite—micromechanical modeling was chosen to predict the viscoelastic behavior of bitumen. In the framework of continuum micromechanics, a homogenization scheme on the basis of the constituents of bitumen identified in SARA fractionation was derived taking micelle structures into account. Thereby, bitumen was considered as a four-phase composite, consisting of a contiguous maltene matrix with embedded spherical asphaltene and saturate inclusions. In addition, needles built up by highly polar aromatics and resins oriented in all directions were implemented to represent the interaction between asphaltene micelles. The volume content of these needles was found to correlate with the asphaltene content in an exponential way, corresponding to a typical rate of growth in natural molecular bonding processes.

The power-law model turned out to describe the viscoleastic creep response of the maltene phase (saturates, aromatics and resins) very well. While the model parameters $J_{0,\mathrm{arom}}$, $J_{\mathrm{a,arom}}$ and k_{arom} of the maltene phase could be determined directly from CR tests, the material behavior of the asphaltenes was back-calculated from experimental results from bitumen artificially composed at different asphaltene contents on a best-fit basis using the coefficient of determination R^2 as an indicator for the degree of accordance. With the material parameters at hand, the multiscale model was used to predict the viscoelastic response of bitumen showing remarkable accordance between experimental and predicted results for various temperatures.

Because of lack of artificial bitumen produced from other bitumens, only the microstructure of one specific paving grade bitumen 70/100 was studied in the course of this work. To examine the microstructure of other bitumens and hence validate the presented micromechanical model appears as interesting and essential task for further research. Moreover, a detailed identification of the behavior of the material phases (e.g. saturates) would lead to a further improvement of the accuracy of model predictions. In addition, the investigation and description of aging effects could be a useful extension of the presented model.

Acknowledgments The authors gratefully acknowledge financial support from the Austrian Research Promotion Agency (FFG) and the sponsors Pittel+Brausewetter, Swietelsky and Nievelt through project "OEKOPHALT—Physical–chemical fundamentals on bitumen aging". They further appreciate the support of Daniel Großegger and Thomas Riedmayer with sample preparation and execution of CR tests.

Appendix 1: Stroud's integration formula

The scalar weights $\omega(\vartheta_j, \varphi_j)$ in Eq. 11 and the orientations ϑ_j and φ_j are defined in Table 5.

Table 5 Scalar weights $\omega(\vartheta_j, \varphi_j)$ and orientations ϑ_j and φ_j for Stroud's integration [32]

j	1	2	3	4	5	6	7	8	9	10	11	12	13	14	15
$\sin(\vartheta_j)\cos(\varphi_j)$	$+r$	$+r$	$-r$	$-r$	$+t$	$+t$	$-t$	$-t$	$+s$	$+s$	$-s$	$-s$	1	0	0
$\sin(\vartheta_j)\sin(\varphi_j)$	$+s$	$-s$	$+s$	$-s$	$+r$	$-r$	$+r$	$-r$	$+t$	$-t$	$+t$	$-t$	0	1	0
$\cos(\vartheta_j)$	$+t$	$+t$	$+t$	$+t$	$+s$	$+s$	$+s$	$+s$	$+r$	$+r$	$+r$	$+r$	0	0	1
$\omega(\vartheta_j, \varphi_j)$	$\frac{1}{15}$	$\frac{1}{15}$	$\frac{1}{15}$	$\frac{1}{15}$	$\frac{1}{15}$	$\frac{1}{15}$	$\frac{1}{15}$	$\frac{1}{15}$	$\frac{1}{15}$	$\frac{1}{15}$	$\frac{1}{15}$	$\frac{1}{15}$	$\frac{1}{15}$	$\frac{1}{15}$	$\frac{1}{15}$

with $r = 1/2$, $s = (\sqrt{5}+1)/4$ and $t = (\sqrt{5}-1)/4$

Appendix 2: Transformation of local Hill's shape tensors into global frame

To sum up the tensors in Stroud's integration formula [32, 40] in Eq. 11, the tensors $\mathbf{P}_{\text{cyl}}^{*,\text{arom}}(\vartheta_j, \varphi_j, \text{p})$ have to be given in the same base frame. While analytical expressions for $\mathbf{P}_{\text{cyl}}$ are available in a local base frame [9, 13] coinciding with the principal axis of the ellipsoid (see Fig. 15), the corresponding components of $\mathbf{P}$ in $[6 \times 6]$ "Kelvin–Mandel" matrix notation, reading as [7, 17, 29]

$$\mathbf{P} = \begin{bmatrix} P_{1111} & P_{1122} & P_{1133} & \sqrt{2}P_{1123} & \sqrt{2}P_{1131} & \sqrt{2}P_{1112} \\ P_{2211} & P_{2222} & P_{2233} & \sqrt{2}P_{2223} & \sqrt{2}P_{2231} & \sqrt{2}P_{2212} \\ P_{3311} & P_{3322} & P_{3333} & \sqrt{2}P_{3323} & \sqrt{2}P_{3331} & \sqrt{2}P_{3312} \\ \sqrt{2}P_{2311} & \sqrt{2}P_{2322} & \sqrt{2}P_{2333} & 2P_{2323} & 2P_{2331} & 2P_{2312} \\ \sqrt{2}P_{3111} & \sqrt{2}P_{3122} & \sqrt{2}P_{3133} & 2P_{3123} & 2P_{3131} & 2P_{3112} \\ \sqrt{2}P_{1211} & \sqrt{2}P_{1222} & \sqrt{2}P_{1233} & 2P_{1223} & 2P_{1231} & 2P_{1212} \end{bmatrix}, \tag{15}$$

can be transformed very efficiently from local frames to one global frame through [29]

$$\mathbf{P}_{cyl,global}^{ef}(\varphi, \vartheta; p) = \mathbf{Q}(\varphi, \vartheta)\mathbf{P}_{cyl,local}^{ef}(p)\mathbf{Q}^{t}(\varphi, \vartheta), \tag{16}$$

with $\mathbf{Q}^{t}(\varphi, \vartheta)$ as the transpose of $\mathbf{Q}(\varphi, \vartheta)$, and

$$\mathbf{e}_1 = \begin{bmatrix} \cos\varphi\cos\vartheta \\ \sin\varphi\cos\vartheta \\ -\sin\varphi \end{bmatrix}, \quad \mathbf{e}_2 = \begin{bmatrix} -\sin\varphi \\ \cos\varphi \\ 0 \end{bmatrix}, \quad \mathbf{e}_3 = \begin{bmatrix} \cos\varphi\sin\vartheta \\ \sin\varphi\sin\vartheta \\ \cos\varphi \end{bmatrix}. \tag{19}$$

The components q_{ij} are the elements of the matrix $\mathbf{q}$ in $\mathbf{Q}$, reading as

$$q_{ij} = [\mathbf{e}_1, \mathbf{e}_2, \mathbf{e}_3], \qquad i = 1\ldots3, \quad j = 1\ldots3, \tag{18}$$

$$\mathbf{Q}(\varphi, \vartheta) = \begin{bmatrix} q_{11}^2 & q_{12}^2 & q_{13}^2 & \frac{2}{\sqrt{2}}q_{12}q_{13} & \frac{2}{\sqrt{2}}q_{13}q_{11} & \frac{2}{\sqrt{2}}q_{11}q_{12} \\ q_{21}^2 & q_{22}^2 & q_{23}^2 & \frac{2}{\sqrt{2}}q_{22}q_{23} & \frac{2}{\sqrt{2}}q_{23}q_{21} & \frac{2}{\sqrt{2}}q_{21}q_{22} \\ q_{31}^2 & q_{32}^2 & q_{33}^2 & \frac{2}{\sqrt{2}}q_{32}q_{33} & \frac{2}{\sqrt{2}}q_{33}q_{31} & \frac{2}{\sqrt{2}}q_{31}q_{32} \\ \sqrt{2}q_{21}q_{31} & \sqrt{2}q_{22}q_{32} & \sqrt{2}q_{23}q_{33} & q_{23}q_{32} + q_{33}q_{22} & q_{21}q_{33} + q_{31}q_{23} & q_{22}q_{31} + q_{32}q_{21} \\ \sqrt{2}q_{31}q_{11} & \sqrt{2}q_{32}q_{12} & \sqrt{2}q_{33}q_{13} & q_{33}q_{12} + q_{13}q_{32} & q_{31}q_{13} + q_{11}q_{33} & q_{32}q_{11} + q_{12}q_{31} \\ \sqrt{2}q_{11}q_{21} & \sqrt{2}q_{12}q_{22} & \sqrt{2}q_{13}q_{23} & q_{13}q_{22} + q_{23}q_{12} & q_{11}q_{23} + q_{21}q_{13} & q_{12}q_{21} + q_{22}q_{11} \end{bmatrix}. \tag{17}$$

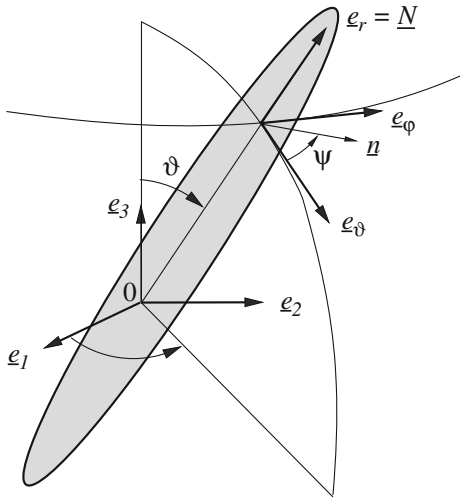

Fig. 15 Cylindrical inclusion representing the interaction of micelles [14]

References

1. Aigner E, Lackner R, Pichler C (2009) Multiscale prediction of viscoelastic properties of asphalt concrete. J Mater Civ Eng (ASCE) 21:771–780
2. ASTM (2010) ASTM D4124-01—standard test methods for separation of asphalt into four fractions. American Society for Testing and Materials International, West Conshohocken
3. Bearsley S, Forbes A, Haverkamp R (2004) Direct observation of the asphaltene structure in paving-grade bitumen using confocal laser-scaning microscopy. J Microsc 215(2):149–155
4. Beurthey S, Zaoui A (2000) Structural morphology and relaxation spectra of viscoelastic heterogeneous materials. Eur J Mech 19(1):1–16
5. Bodan A (1982) Polyquasispherical structure of petroleum asphalts. Chem Technol Fuels Oils 18:614–618
6. Corbett L (1969) Composition of asphalt based on generic fractionation, using solventdeasphaltening, elution-adsorption chromatography and densimetric characterization. Anal Chem 41:576–579
7. Cowin S (2003) A recasting of anisotropic poroelasticity in matrices of tensor components. Transp Porous Media 50:35–56
8. Donolato C (2002) Analytical and numerical inversion of the laplace-carson transform by a differential method. Comput Phys Commun 145:298–309
9. Eshelby J (1957) The determination of the elastic field of an ellipsoidal inclusion, and related problems. Proc R Soc Lond Ser A 241:376–396
10. Espinat D, Rosenberg E, Scarsella M, Barre L, Fenistein D, Broseta D (1998) Colloidal structural evolution from stable to flocculated state of asphaltene solutions and heavy crudes. Planum Press, New York, pp 145–201
11. Forbes A, Haverkamp R, Robertson T, Bryant J, Bearsley S (2001) Studies of the microstructure of polymer-modified bitumen emulsions using confocal laser scanning microscopy. J Microsc 204(3):252–257
12. Fritsch A, Hellmich C (2007) 'Universal' microstructural patterns in cortical and trabecular, extracellular and extravacular bone materials: Micromechanics-based prediction of anisotropic elasticity. J Theor Biol 244:597–620
13. Fritsch A, Dormieux L, Hellmich C, Sanahuja J (2009a) Mechanical behaviour of hydroxyapatite biomaterials: an experimentally validated micromechanical model for elasticity and strength. J Biomed Mater Res A 88A:149–161
14. Fritsch A, Hellmich C, Dormieux L (2009b) Ductile sliding between mineral crystals followed by rupture of collagen crosslinks: experimentally supported micromechanical explanation of bone strength. J Theor Biol 260(2):230–252
15. Füssl J, Lackner R, Eberhardsteiner J (2013) Creep response of bituminous mixtures—rheological model and microstructural interpretation. Meccanica. doi:10.1007/s11012-013-9775-y
16. Handle F, Füssl J, Neudl S, Grossegger D, Eberhardsteiner L, Hofko B, Hospodka M, Blab R, Grothe H (2013) Understanding the microstructure of bitumen: a CLSM and fluorescence approach to model bitumen ageing behavior. In: Proceedings to 12th ISAP International Conference on Asphalt Pavements, Raleigh, USA, 2014
17. Helnwein P (2001) Some remarks on the compressed matrix representation of symmetric second-order and fourth-order tensors. Comput Methods Appl Mech Eng 190(22–23): 2753–2770
18. Hill R (1963) Elastic properties of reinforced solids: some theoretical principles. J Mech Phy Solids 11:357–362
19. Hill R (1965) Continuum micro-mechanics of elastoplastic polycrystals. J Mech Phy Solids 13(2):89–101
20. Hofstetter K, Hellmich C, Eberhardsteiner J (2005) Development and experimental validation of a continuum micromechanics model for the elasticity of wood. Eur J Mech 24:1030–1053
21. Lackner R, Blab R, Jäger A, Spiegl M, Kappl K, Wistuba M, Gagliano B, Eberhardsteiner J (2004) Multiscale modeling as the basis for reliable predictions of the behavior of multicomposed materials. In: Topping B, Soares CM (eds) Progress in engineering computational technology, vol 8. Saxe-Coburg Publications, Stirling, pp 153–187
22. Lackner R, Spiegl M, Eberhardsteiner J, Blab R (2005) Is the low-temperature creep of asphalt mastic independent of filler shape and mieralogy? Arguments from multiscale analsysis. J Mater Civ Eng (ASCE) 17(5):485–491
23. Laws N (1977) The determination of stress and strain concentrations at an ellipsoidal inclusion in an anisotropic material. J Elasticity 7(1):91–97
24. Laws N, McLaughlin R (1978) Self-consistent estimates for the viscoelastic creep compliances of composite materials. Proc R Soc Lond Ser A 359:251–273
25. Lesueur D (2009) The colloidal structure of bitumen: consequences on the rheology and on the mechanisms of bitumen modification. Adv Colloid Interface Sci 145:42–82
26. Lu X, Langton M, Olofsson P, Redelius P (2005) Wax morphology in bitumen. J Mater Sci 40:1893–1900
27. Mang H, Pichler B, Bader T, Füssl J, Jia X, Fritsch A, Eberhardsteiner J, Hellmich C (2012) Quantification of structural and material failure mechanisms across different

length scales: from instability to brittle-ductile transitions. Acta Mech 223:1937–1957
28. Mori T, Tanaka K (1973) Average stress in matrix and average elastic energy of materials with misfitting inclusions. Acta Metall 21(5):571–574
29. Nadeau J, Ferrari M (1998) Invariant tensor-to-matrix mappings for evaluation of tensorial expressions. J Elasticity 52:43–61
30. Nahar S, Schmets A, Scarpas A, Schitter G (2013) Temperature and thermal history dependence of the microstructure in bituminous materials. Eur Polym J 49:1964–1974
31. Pichler C, Lackner R (2009) Upscaling of viscoelastic properties of highly-filled composites: investigation of matrix-inclusion type morphologies with power-law viscoelastic material response. Compos Sci Technol 69:2410–2420
32. Pichler B, Hellmich C, Eberhardsteiner J (2009) Spherical and acicular representation of hydrates in a micromechanical model for cement paste: prediction of early-age elasticity and strength. Acta Mech 203:137–162
33. Pichler C, Lackner R, Aigner E (2012) Generalized self-consistent scheme for upscaling of viscoelastic properties of highly-filled matrix-inclusion composites - application in the context of multiscale modeling of bituminous mixtures. Composites 43:457–464
34. Read W (1950) Stress analysis for compressible viscoelastic media. J Appl Phys 21(7):671–674
35. Richardson C (1910) The modern asphalt pavement. Wiley, New York
36. Rostler F (1965) Fractional composition: analytical and functional significance, vol 2. Interscience Publishers, New York
37. Scheiner S, Hellmich C (2009) Continuum microviscoelasticity model for aging basic creep of early-age concrete. J Eng Mech 135(4):307–323
38. Sips R (1951) General theory of deformation of viscoelastic substances. J Polym Sci 7(2–3):191–205
39. Stehfest H (1970) Algorithm 368: numerical inversion of laplace transforms. Commun ACM 13:47–49
40. Stroud A (1971) Approximate calculation of multiple integrals. Prentice-Hall, Englewood Cliffs
41. Suquet P (ed) (1997) Continuum micromechanics. Springer, Wien
42. Wakashima K, Tsukamoto H (1991) Mean-field micromechanics model and its application to the analysis of thermomechanical behaviour of composite materials. Mater Sci Eng A 146(1–2):291–316
43. Yen T (1992) The colloidal aspect of a macrostructure of petroleum asphalt. Fuel Sci Technol Int 10:723–733
44. Zaoui A (1997) Structural morphology and constitutive behavior of microheterogeneous materials. In: Suquet P (ed) Continuum micromechanics. Springer, Wien, pp 291–347
45. Zaoui A (2002) Continuum micromechanics: survey. J Eng Mech (ASCE) 128(8):808–816